Published in final edited form as:
Mol Psychiatry. 2025 February ; 30(2): 367–378. doi:10.1038/s41380-024-02680-9.

Neural circuit mechanisms underlying aberrantly prolonged functional hyperemia in young Alzheimer's disease mice

Thomas A. Kim[1,2], **George Cruz**[2], **Michelle D. Syty**[3], **Faye Wang**[3], **Xinxing Wang**[3], **Alexandra Duan**[3], **Marc Halterman**[4], **Qiaojie Xiong**[3,*], **Jorge J. Palop**[5,6,*], **Shaoyu Ge**[3,*]

[1]Medical Scientist Training Program (MSTP), Renaissance School of Medicine at Stony Brook University

[2]Program in Neuroscience, Stony Brook University, Stony Brook, NY, 11794, USA

[3]Department of Neurobiology and Behavior, Stony Brook University, Stony Brook, NY, 11794, USA

[4]Department of Neurology, Stony Brook University, Stony Brook, NY, 11794, USA

[5]Gladstone Institute of Neurological Disease, San Francisco, CA, 94158, USA

[6]Department of Neurology, University of California, San Francisco, CA, 94158, USA

Abstract

Neurovascular defects are one of the most common alterations in Alzheimer's disease (AD) pathogenesis, but whether these deficits develop before the onset of amyloid beta (Aβ) accumulation remains to be determined. Using *in vivo* optical imaging in freely moving mice, we explored activity-induced hippocampal microvascular blood flow dynamics in App^{SAA} knock-in and J20 mouse models of AD at early stages of disease progression. We found that prior to the onset of Aβ accumulation, there was a pathologically elevated blood flow response to context exploration, termed functional hyperemia. After the onset of Aβ accumulation, this context exploration–induced hyperemia declined rapidly relative to that in control mice. Using *in vivo* electrophysiology recordings to explore the neural circuit mechanism underlying this blood flow alteration, we found that hippocampal interneurons before the onset of Aβ accumulation were hyperactive during context exploration. Chemogenetic tests suggest that hyperactive activation of inhibitory neurons accounted for the elevated functional hyperemia. The suppression of nitric oxide (NO) produced from hippocampal interneurons in young AD mice decreased the accumulation of Aβ. Together, these findings reveal that neurovascular coupling is aberrantly elevated before Aβ deposition, and this hyperactive functional hyperemia declines rapidly upon Aβ accumulation.

---

[*] Correspondence should be addressed to: Shaoyu Ge, PhD, Department of Neurobiology and Behavior, Stony Brook University, Stony Brook, NY, 11794, USA, shaoyu.ge@stonybrook.edu.
Alternatively, correspondence can be addressed to Drs. Palop or Xiong
Author contributions
Conceptualization, T.A.K. and S.G.; Methodology, T.A.K and S.G.; Formal Analysis, T.A.K., G.C., M.D.S., and F.W.; Investigation, T.A.K., G.C., M.D.S., X.W, and F.W.; Writing, T.A.K. and S.G. produced the initial manuscript, and all others reviewed and commented on the manuscript; Supervision, Q.X. and S. G.; Funding Acquisition, S.G., J.J.P, Q.X.

Conflicts of interest: The authors have no relevant conflicts of interest.

Disclosures: The authors have no relevant disclosures.

Introduction

Functional hyperemia, also known as neurovascular coupling, refers to a local increase in blood flow by the dilation of blood vessels in response to increased metabolic activity in a brain area(1, 2). It is a critical brain function that maintains brain metabolic homeostasis by delivering oxygen and glucose to the brain as well as clearing the brain of toxic waste and metabolic byproducts such as amyloid-β (Aβ) peptide, lactate, and carbon dioxide(1). Studies in Alzheimer's disease (AD) patients using functional magnetic resonance imaging (fMRI) show impairments in functional hyperemia due to a loss of medial temporal lobe and hippocampus activation(3–5). A multifactorial data-driven analysis of various neuroimaging techniques in late-onset AD patients demonstrates that vascular dysfunction is a crucial pathological event during the early stages of disease development(6). Furthermore, vascular risk factors including blood-brain barrier disruption, genetics, hypertension, heart disease, and diabetes as well as stroke may contribute to the development of AD pathology(7–9). Although these studies suggest that vascular dynamics play an essential role in the progression of AD symptoms, the function of vascular dynamics before the onset of Aβ accumulation remains to be determined.

Cardiac rhythm activity is generally considered to be the driving force of systemic hemodynamics. However, accumulating evidence reveals that cerebrovascular dynamics, such as blood flow velocity, are regulated by neuronal circuit activity(1, 2). The use of fMRI and Doppler fluxmetry to analyze functional hyperemia and cerebral blood flow reveals a decline in brain activity-induced hyperemia of cerebral vessels with aging and AD(10–20). These emerging findings raise the question of whether neuronal activity-induced microvascular dynamics are altered prior to Aβ accumulation and contribute to AD pathogenesis.

Mechanistic studies of neuronal activity-induced microvascular dynamics suggest that both excitatory and inhibitory neurons are involved in regulating functional hyperemia(2, 21–26). In a recent study, we found that context exploration–induced activation of hippocampal inhibitory neurons in mice leads to functional hyperemia in the dentate gyrus (DG)(26). Moreover, this increased blood flow is at least partially due to elevated production of NO by inhibitory neurons(26). Interestingly, aberrant neuronal network activity, such as impairments in interneurons, is commonly reported to account for cognitive deficits in AD patients and mouse models(27–35). These studies lead to the question of whether there are alterations in interneuron activity prior to AD diagnosis that might further affect functional hyperemia.

In this study, we analyzed functional hyperemia in the hippocampus of App^{SAA} knock-in (AppKI) and J20 AD mouse models before and after the onset of AD pathogenesis and explored the underlying neural circuit mechanisms. Using *in vivo* optical imaging, we analyzed hippocampal microvascular blood flow dynamics in young and old AD mouse models. We found that before Aβ accumulation, there was aberrantly prolonged functional hyperemia in response to novel context exploration relative to age-matched control mice. *In vivo* electrophysiology recordings of hippocampal neuronal activity during context exploration revealed continuously elevated activation of interneurons prior to Aβ accumulation. Chemogenetic activation of inhibitory neurons was sufficient to induce hyperemia, which was suppressed by inhibition of NO production. This suggests that hyperactive inhibitory neuronal activation accounts for increased functional hyperemia prior to Aβ accumulation in AD mice. Importantly, inhibiting neurovascular coupling by suppressing NO production decreased the burden of Aβ accumulation, shedding light on the physiological significance of aberrantly prolonged functional hyperemia.

Results

Aberrantly prolonged functional hyperemia in the hippocampus of 3-month-old AppKI mice induced by context exploration

Dysfunctional vascular dynamics have recently been considered a key cause of brain degeneration(8, 36). In contrast to studies of impairments in functional hyperemia after disease diagnosis, impairments prior to diagnosis remain largely unexplored. In this study, we used AD mouse models to analyze functional hyperemia in the hippocampus before and after the onset of AD pathogenesis and explored the underlying neural circuit mechanisms.

Pathological hallmarks of AD include the presence of Aβ plaques and neurofibrillary tangles(37). We first analyzed the timeline and distribution of Aβ accumulation in the hippocampus of AppKI mice(38) at 2, 3, 4, 5, 6, and 9 months of age. We observed incipient Aβ accumulation in the hippocampus starting at 4 months of age followed by a sharp increase in Aβ pathology (Fig. 1A, B), consistent with previous findings in this and other AppKI mouse lines(38, 39). We then quantified Aβ accumulation in each subfield of the hippocampus, including the DG, Cornu Ammonis 1 (CA1), and CA2/CA3. All subfields progressively showed age-dependent accumulation of Aβ starting at 4 months of age (Fig. 1B). We further analyzed Aβ accumulation in individual laminae of the DG. Although there was no detectable Aβ signal at 3 months of age, there was strong Aβ accumulation in all laminae by 6 months of age (Fig. 1C).

To directly analyze functional hyperemia in the hippocampus of AD mice, we used an *in vivo* recording paradigm with optical methods as previously described(26) (Fig. 2A). Briefly, we injected an adeno-associated virus (AAV) expressing green fluorescent protein (GFP) into the DG of adult mice, followed by implantation of a gradient refractive index (GRIN) lens. Three weeks later, we captured fluorescent images of the DG with an Inscopix miniature microscope. Using the contrast of optical signals between red blood cells (RBCs) and plasma, we obtained direct measurements of blood flow by analyzing the movement of plasma through a given microvessel (Fig. 2B, top). The slope of the movement of plasma (pixels/time) was measured as an index of blood flow velocity (Fig. 2B, bottom).

Before analyzing activity-induced hyperemia in AD mice, we measured context exploration–induced microvascular blood flow velocity in 3-month-old wild-type (WT) mice. We first recorded from mice for 10 min in their home cage (HC) containing only bedding to establish baseline blood flow velocity. We then performed recordings in an enriched environment (EE) cage containing 5–6 objects to promote context exploration for 70 min. We performed 1-min recordings every 3 min during baseline followed by a 10-min continuous recording.

After the first 10 min, we recorded 1 min every 10 min to avoid possible photobleaching. The following day, recordings were made while mice were in their HC for the first 10 min to establish a baseline and then 70 min still in their HC as a control. We observed a robust increase in blood flow velocity during the first 10 min of EE exploration, which returned to baseline levels within 40 min (Fig. 2C, left), consistent with our previous report(26). We next examined the context exploration–induced elevation of microvascular blood flow velocity in 3-month-old AppKI mice, which lacked detectable Aβ accumulation. Using the same viral infusion, lens implantation, and recording procedures, we observed elevated flow velocity in the first 10 min (Fig. 2C, right), similar to that observed in WT mice. Surprisingly, in 3-month-old AppKI mice, the EE-induced increase in flow velocity remained elevated after 1 h (Fig. 2C, right), indicative of aberrantly prolonged functional hyperemia.

To examine whether this aberrantly prolonged activation of functional hyperemia in response to EE also occurs in other AD mouse lines, we measured microvascular flow velocity under EE in the J20 mouse model(40), which does not have detectable Aβ plaque accumulation until 4–5 months of age(41, 42). Consistent with our findings in 3-month-old AppKI mice, we observed aberrantly prolonged hyperemia in response to EE in 3-month-old J20 mice (Supple. Fig. 1A, left). To further analyze the EE-induced increase in blood flow velocity in WT, AppKI, and J20 mice, we quantified the average fold change of blood flow velocity during 1–10 min, 20–40 min, and 60–70 min of EE. There were comparable EE-induced elevations of functional hyperemia during 1–10 min in all three groups (Fig. 2D). However, elevations during 20–40 min and 60–70 min were observed in AppKI and J20 mice but not WT mice (Fig. 2E, F). To exclude the possibility that the change in functional hyperemia was due to altered exploration activity, we analyzed the traveling distance of mice. There were no detectable differences in traveling distance among WT, AppKI, and J20 mice under HC or EE conditions (Supple. Fig. 2A–E).

Accelerated decline of context exploration–induced hyperemia in aging AppKI mice

Brain activity-induced hyperemia is reduced in AD patients(43–45). Thus, the finding that AD mice showed aberrantly prolonged EE-induced hyperemia prior to Aβ accumulation led us to examine functional hyperemia in these mice after the onset of detectable accumulation of Aβ.

We first assessed functional hyperemia during healthy aging in 6- and 9-month-old WT mice. The EE-induced alteration of blood flow velocity during the first 40 min remained elevated in 6-month-old WT mice (Fig. 3A, left), similar to that observed at 3 months of age. However, in 9-month-old WT mice, blood flow velocity fell back to baseline levels within 10 min (Fig. 3A, right). We next examined EE-induced hyperemia in 6- and 9-month-old AppKI mice. 6-month-old AppKI mice showed a return of blood flow velocity to baseline levels within 10 min (Fig. 3B, left). EE-induced functional hyperemia was barely detectable in 9-month-old AppKI mice (Fig. 3B, right).

To statistically compare the reductions in EE-induced hyperemia during aging between WT and AppKI mice, we measured the amplitudes of EE-induced hyperemia during 1–10 min and 20–70 min of EE. 3-month-old WT mice had a higher increase in blood flow velocity than 6- and 9-month-old WT mice during 1– 10 min, with no sharp decrease between 6- and 9-month-old mice (Fig. 3C). However, the amplitudes of functional hyperemia during 20–70 min of EE were similar between 3- and 6-month-old mice and were lower in 9-month-old mice, which showed no increase in blood flow velocity during this period (Fig. 3D). These observations indicate a progressive decline in brain activity-induced hyperemia in aging WT mice (Fig. 3C, D). In aging AppKI mice, EE-induced hyperemia declined substantially during the first 10 min of EE (Fig. 3E). An elevation of EE-induced hyperemia between 20–70 min was observed in 3-month-old AppKI mice (Fig. 3F) but not in 6- and 9-month-old AppKI mice. The traveling distance of these mice was comparable in both HC and EE conditions (Supple. Fig. 2A, B; Supple. Fig. 3A–H). To further determine whether this effect is specific to certain transgenic mice, we analyzed EE-induced hyperemia in 6-month-old J20 mice. Similar to that observed in 6-month-old AppKI mice, the EE-induced elevation of blood flow velocity returned to baseline levels within 20 min in 6-month-old J20 mice (Supple. Fig. 1A, right).

Taken together, these findings reveal that prior to detectable Aβ accumulation, context exploration induced aberrantly prolonged functional hyperemia in the hippocampus of AppKI mice. Importantly, compared with WT mice, aging AD mice showed accelerated decline of context exploration–induced hyperemia as Aβ accumulated.

Chemogenetic activation of hippocampal inhibitory neurons induced similar hyperemia in 3- and 6-month-old AppKI mice

The accelerated decline in functional hyperemia observed in aging AppKI mice led us to speculate whether neurovascular coupling machinery becomes less functional with age. In the hippocampus of adult mice, we recently found that EE activates hippocampal inhibitory neurons and that this activation is responsible for elevated functional hyperemia(26). To assess the function of neurovascular coupling machinery, we thus activated hippocampal interneurons and analyzed microvascular blood flow velocity in AppKI mice.

We first activated hippocampal inhibitory neurons and analyzed blood flow velocity in 3-month-old AppKI mice, which lacked detectable Aβ accumulation. In 3-month-old AppKI mice, we expressed hM3Dq (Gq), an excitatory designer receptor exclusively activated by a designer drug (DREADD), tagged with dTomato in hippocampal interneurons by injecting AAV9-hDlx-GqDREADD(46) into the DG. The hDlx promoter was used to specifically express the transgenes in interneurons (Fig. 4A). AAV9-CAG-GFP was co-injected to express GFP for analyzing blood flow velocity. Three weeks after viral injection and lens implantation, we recorded inhibitory neuron activity-induced blood flow velocity (Fig. 4B). After the baseline recording, we injected mice with saline as a control and administered the DREADD ligand JHU37160(47) (0.5 mg/kg, i.p.) the following day. Microvascular blood flow was recorded for 3 min every 10 min for up to 30 min post-injection. Afterward, mice were sacrificed to verify the injection site. Measurements were averaged over each 3-min recording and plotted against the recording time (Fig. 4C). JHU37160-induced activation of interneurons in the DG substantially increased blood flow velocity as early as 10 min post-injection. The elevation of microvascular blood flow velocity by JHU37160 persisted for the entire 30 min (Fig. 4C). As expected, there was no detectable change during the recording time window in saline-injected control mice. During these experiments, there was no detectable difference in traveling distance between saline- and JHU37160-injected mice (Supple. Fig. 4A).

We next examined inhibitory neuronal activation-induced hyperemia in 6-month-old AppKI mice. We found that JHU37160-induced activation of interneurons in the DG of 6-month-old AppKI mice also substantially increased blood flow velocity starting 10 min post-injection and lasting throughout the 30-min recording. There was no detectable change during the recording time window in saline-injected controls (Fig. 4D). Interestingly, the amplitude of the elevated blood flow velocity was similar to that in 3-month-old AppKI mice (Fig. 4E). Traveling distance was similar between saline- and JHU37160-injected mice (Suppl. Fig. 4B).

Furthermore, to exclude the possibility of potential changes in blood flow velocity due to the JHU37160 drug itself, we injected JHU37160 into mice infected with only AAV9-CAG-GFP. As expected, blood flow velocity after injection of JHU37160 was comparable to that after injection of saline (Fig. 4F), and there was no difference in traveling distance between groups (Supple. Fig. 4C).

The activation of inhibitory neurons increases blood flow at least partially through NO signaling, which can be blocked by inhibition of neuronal isoform of nitric oxide synthase (nNOS) with omega-nitro-L-arginine methyl ester (L-NAME)(26). In adult AppKI mice expressing AAV9-hDlx-GqDREADD in the DG, we injected L-NAME (30 μg/g, i.p.) 20 min prior to JHU37160 injection and analyzed mice for 30 min after JHU37160 injection. L-NAME injection was sufficient to abolish JHU37160-induced hyperemia in adult AppKI mice compared with JHU37160-only injected mice (Fig. 4G). The traveling distance between groups did not differ (Supple. Fig. 4D).

These findings show that interneuron activity induced similar elevation of microvascular blood flow velocity in the hippocampus of 3- and 6-month-old AppKI mice. This suggests that the coupling machinery between the interneuron network and microvasculature in 6-month-old AppKI mice is functionally similar to that of 3-month-old mice.

Hyperactivation of hippocampal interneurons during context exploration in young AppKI mice

The observation that chemogenetic activation of inhibitory neurons induced similar hyperemia in 3- and 6-month-old AppKI mice led us to explore possible neuronal mechanisms underlying aberrantly prolonged EE-induced hyperemia. We employed tetrode recordings in 3-month-old AppKI and WT mice to analyze inhibitory neuronal firing in the hippocampus under both HC and EE conditions. Two weeks after implanting a tetrode in the DG, we recorded neuronal activity from each mouse in HC for 20 min, followed by 1-h recording in EE (Fig. 5A). After the experiments, mice were sacrificed to verify the tetrode implantation site, and only mice with the correct location were included in the analysis (Supple. Fig. 5A).

We then classified the recorded units as excitatory DG cells (DGCs) or inhibitory neurons according to their waveform symmetry index, waveform width, and long-term firing rate(48). Firing frequencies across HC and EE conditions were analyzed and plotted (Fig. 5B, C; Supplementary Figure 5B). In 3-month-old WT mice, interneurons increased their firing rate during exploration (Fig. 5D, E), consistent with a previous report(48). The elevation in firing rate was obvious during the first 20 min of EE and returned to baseline between 40–60 min (Fig. 5F, G). In 3-month-old AppKI mice, the firing rate of interneurons increased robustly in response to EE (Fig. 5H, I). This elevation remained throughout the entire 1-h exploration period (Fig. 5J, K). We next examined the DGC firing rate in WT and AppKI mice. In WT mice, DGCs decreased their firing rate in response to EE (Supple. Fig. 5C–E), as previously reported(48). Interestingly, we did not detect a change in DGC firing rate during EE in AppKI mice (Supple. Fig. 5F–H).

In summary, tetrode recordings of inhibitory and excitatory neurons in the DG revealed prolonged elevation of interneuron activation during EE in 3-month-old AppKI mice compared with age-matched WT mice. This sustainable activation of inhibitory neurons during EE might account for the aberrantly prolonged EE-induced functional hyperemia in 3-month-old AppKI mice.

Suppression of hyperactive functional hyperemia decreased Aβ accumulation in young AppKI mice

The observation that hyperactive inhibitory neuron activity induces prolonged functional hyperemia in young AppKI mice leads us to suspect whether this prolonged hyperemia disrupts brain metabolic homeostasis, potentially promoting Aβ accumulation. We therefore explored whether suppression of hyperactive functional hyperemia in young AppKI mice affects Aβ accumulation. Thus, we examined Aβ signal in AppKI mice at 4 months of age, when Aβ starts to accumulate in the hippocampus, after suppressed functional hyperemia. L-NAME efficiently inhibits brain activity-indued hyperemia in adult mice (26), and inhibitory neuron activation-induced hyperemia in young AppKI mice (Fig. 4G). We first confirmed the effect of L-NAME on functional hyperemia in young freely behaving AppKI mice, showing an obvious reduction when L-NAME was applied (Supple. Fig. 6). We then used LNAME to suppress hyperactive functional hyperemia and determined its role in regulating Aβ accumulation. AppKI mice received L-NAME orally through drinking water at a concentration of 100 mg/kg for 3 days or standard drinking water as a control. We then performed immunostaining for Aβ in hippocampal slices (Fig. 6A). We observed that Aβ accumulation in the hippocampus, especially in the DG, was reduced in L-NAME treated group compared with the control group (Fig. 6B, C).

Next, we examined how these treatments affected Aβ accumulation in 6-month-old AppKI mice (Supple. Fig. 7A). Similar to the 4-month-old AppKI mice, we observed a decline in Aβ accumulation with L-NAME treatment (Supple. Fig. 7B, C). However, in contrast to the 4-month-old AppKI mice, we observed that the treatment of L-NAME became less effective to decrease the Aβ accumulation in the hippocampus and DG.

Taken together, these observations show that inhibition of the effect of neural circuit activity on vascular dynamics through L-NAME decreased the accumulation of Aβ in at least young and adult AppKI mice.

Discussion

In this study, using *in vivo* optical imaging, we analyzed context exploration–induced microvascular blood flow dynamics, termed functional hyperemia, in AD mouse models across aging. We found aberrantly prolonged elevation of functional hyperemia during context exploration in the hippocampus of AD mice prior to the onset of Aβ accumulation. By contrast, in age-matched WT mice, the elevation of activity-induced hyperemia was transient. Moreover, we observed an accelerated decline of context exploration–induced functional hyperemia in AD mice compared with age-matched WT mice. Importantly, using tetrode recordings, we found that hippocampal interneurons in AD mice were tonically activated during context exploration before the onset of Aβ accumulation. Lastly, suppression of functional hyperemia with L-NAME delayed Aβ accumulation in the hippocampus of AD mice.

Changes in functional hyperemia in models of AD and aging are well-defined in both humans and mice(18, 49, 50). However, changes in functional hyperemia prior to AD pathogenesis have yet to be carefully investigated. Imaging cerebral blood flow in awake animals has always been challenging, especially with high spatiotemporal resolution. Therefore, using a recently established optical imaging method in freely moving mice, we were able to examine the neural circuit mechanisms underlying altered functional hyperemia in the hippocampus of AD and aging mice. Surprisingly, we found that context exploration induced aberrantly prolonged functional hyperemia in the hippocampus of 3-month-old AD mice, but a rapid decline in functional hyperemia occurred with aging and Aβ accumulation. This finding of a decline in functional hyperemia is consistent with observations made in AD patients(18–20).

What is the consequence of early-age hyperactive functional hyperemia? Functional hyperemia is a type of brain activity that maintains brain metabolic homeostasis, during which there is a hemodynamic response to neuronal activity to supply neural circuits with more oxygen and nutrients(1, 2). Meanwhile, metabolic waste and other cellular products like Aβ are removed from neural circuits(1, 2). One would expect that a reduction in functional hyperemia would lead to a deficiency of nutrient supplies during brain activity and, importantly, accumulation of Aβ in the brain. In AD patients and mice, it is commonly assumed that vascular and functional hyperemia dysfunction occurs due to and after the accumulation of Aβ(18–20, 51–55). However, recent studies show that Aβ is not necessarily strictly correlated with this decline(56–58). These findings further suggest that Aβ is not the sole cause of dysregulated functional hyperemia. Similarly, our present observations show aberrantly prolonged functional hyperemia in pre-amyloid-stage AD mice, suggesting that Aβ does not necessarily warrant functional hyperemia dysfunction. Our study then brings into question the role of functional hyperemia early in the course of hippocampal Aβ accumulation in AD.

The observation that pronounced functional hyperemia precedes A-β accumulation led us to hypothesize whether prolonged hyperemia disrupts brain metabolic homeostasis. We speculate that it disrupts blood flow, potentially leading to an influx of metabolites into brain circuits. This excess could cause imbalanced metabolic activity, possibly a form of hyperglycolysis, driven by hyperactive inhibitory neurons. Such imbalance `s suggest dysfunctional metabolic homeostasis even before Aβ accumulates, potentially contributing to its pathological development in AD. To fully understand the link between hyperactive functional hyperemia and Aβ accumulation, we might need metabolomic analyses to obtain a comprehensive metabolic profile of AppKI mice compared to age-matched controls. Additionally, future studies investigating functional hyperemia after Aβ injection into the hippocampus of wild-type mice could provide insights into the causal relationship between local Aβ concentrations and declines in hyperemia throughout AD progression. Finally, while our study focused on the hippocampus, understanding whether aberrantly prolonged functional hyperemia occurs in other brain regions of AD mice could offer further mechanistic insights into the role of hyperemia in the neuroanatomical spread of AD.

Neurovascular coupling signaling is mediated primarily by the vasoactive metabolites of arachidonic acid, NO, and potassium(1). In a recent study, we found that inhibitory neurons are activated during context exploration and, importantly, nNOS-positive neurons among parvalbumin-expressing neurons may play a major role in controlling exploration-induced hyperemia in adult WT mice(26). Consistently, both 3- and 6-month-old AppKI mice showed a robust increase in blood flow velocity with interneuron activation. Moreover, suppression of NO signaling with L-NAME abolished the increase in blood flow velocity due to interneuron activation. Despite strong evidence that NO signaling is the main factor, our study is limited in that we examined the entire interneuron population, despite that different subtypes of interneurons could play distinct roles in functional hyperemia. Somatostatin-, parvalbumin-, and calretinin-expressing interneurons all exhibit functional deficits in different AD models and AD patients(59). Additional studies of the effect of specific interneuron subtypes on functional hyperemia may provide more insight into their roles in regulating functional hyperemia. Furthermore, the neurovascular unit is comprised of various cell types, including astrocytes and microglia. How these different cell types may affect functional hyperemia before and after Aβ accumulation in AD mice remains to be studied.

Consistent with our observation of aberrantly prolonged functional hyperemia in 3-month-old AD mice, we found sustainable activation of interneurons in the DG of AD mice during context exploration. By contrast, only a transient increase was found in 3-month-old WT mice. Therefore, hyperactivation of inhibitory neurons during context exploration is a possible mechanism for aberrantly prolonged functional hyperemia in AD mice. In a side-by-side comparison of baseline firing frequencies of interneurons and DGCs, firing frequencies were lower in AppKI mice than in WT mice (Supple. Fig. 5I, J). Therefore, aberrantly prolonged activation of interneurons may compensate for the decreased activity of interneurons, allowing the brain to maintain metabolic homeostasis. During brain maturation and aging, the formation of Aβ could impair interneuron activity and cause a rapid decline in functional hyperemia. This raises the possibility that mild elevation of interneuron activity during aging may delay the decline in functional hyperemia.

Inhibition of functional hyperemia with L-NAME in young AppKI mice decreased the amount of Aβ accumulation in the DG of young AppKI mice. In a previous study, we found that in wild type of adult, L-NAME decreases but does not have a significant effect on functional hyperemia. When we performed the same tests in young AppKI mice, in which we found there is hyperactive hyperemia. L-NAME successfully suppressed functional hyperemia (Supple. Fig. 6). The suppression of hyperactive functional hyperemia will likely counter dysfunctional metabolic homeostasis, which slows down the onset of A-β accumulation. A brief treatment in 6–7 months old AppKI mice (Supple. Fig. 7) showed a decrease of A-β accumulation although the effect was not as substantial as that with 4-month-odl AppKI mice. Based on the analysis in Figure 1, the accumulation of A-β becomes optically visible in ~4-month-old AppKI mice. The increase remains at an extreme rate till 9 months old. At a later stage such as in 18 months old AppKI mice at which stage the A-β accumulation is already substantia, that whether L-NAME treatment is effective will be interesting to test out in our next step study. However, we should point it out, the L-NAME treatment even with 14 days' treatment, we found that A-β accumulation was just proportionally decreased (data not shown). The A-β accumulation seems not to be able to be stopped.

Interestingly, many studies show an increased level of NO or nNOS in AD patients and mice(60, 61). However, our observations show that inhibition of nNOS reduces Aβ in young AppKI mice at an age when there is aberrantly prolonged functional hyperemia. Similarly, a previous study reports that early inhibition of inducible NOS prior to AD manifestation provides protection against AD pathogenesis(62). As such, transient suppression of nNOS with L-NAME before Aβ plaque formation may provide an alternative way to reduce Aβ accumulation. However, prolonged exposure to L-NAME can have the opposite effect of increasing Aβ accumulation in AD mice(63). This may be because once functional hyperemia declines, further suppression causes elevated Aβ accumulation. Altogether, these findings provide a novel perspective on the neural circuit mechanisms underlying aberrantly prolonged functional hyperemia in the early AD brain. In addition, these results suggest that interventions that normalize changes in hyperemia during pre-symptomatic and early stages of AD may ultimately have therapeutic benefits.

Materials and Methods

Animals

The Stony Brook University Institutional Animal Care and Use Committee (IACUC) monitored the Division of Laboratory Animal Resources and housed and maintained all mice. All surgeries and experimental procedures on mice were approved by the Stony Brook University IACUC and followed guidelines provided by the National Institutes of Health. Surgeries were conducted on mice 1 month prior to experiments. Male and female 3-, 6-, and 9-month-old C57BL/6J (The Jackson Laboratory, strain #000664) and AppKI (The Jackson Laboratory, strain #034711) mice as well as 3- and 6-month-old J20 mice (MMRCC, strain #034836-JAX) were used to measure blood flow velocity. All mice were housed and maintained on a 12-hour light/dark cycle. Mice were provided *ad libitum* access to food and water.

In vivo blood flow recording

AAV9-CAG-GFP virus (Addgene) and AAV9-hDLX-GqDREADD-dTomato-Fishell-4 (Addgene) were stereotaxically injected into the dorsal DG as previously described(26, 64). Briefly, mice were anesthetized with 5% isofluorane and maintained on 1% isofluorane. Virus was injected at DV: 2.5 mm, AP: −2.0 mm, and ML: ±1.4 mm. After 1 week of viral expression, a lens probe (outer diameter: 1.0 mm, length: 4.0 mm, numerical aperture: 0.5) was implanted ~200 μm above the granule cell layer. Three weeks later, a microscope baseplate was fixed to an optimized focal plane on top of the lens probe. All blood flow imaging videos were recorded using a miniature microscope and the nVista data acquisition system (Inscopix, Palo Alto, CA) at a frame rate of 60 Hz. Cells expressing GFP in the DG generated background illumination allowing blood vessels to be highlighted. The difference in fluorescent absorption of RBCs and plasma created a contrast allowing plasma to be observed as white. After experiments, mice were perfused for confirmation of the lens implantation site.

Data processing and analysis

Blood flow velocity in microvessels was analyzed as previously described(26). Briefly, videos were processed, motion-corrected, and exported through Inscopix Data Processing Software. A MATLAB-based algorithm was used to extract and plot pixels from selected vessels on a DMap in relation to time. The x-axis of the DMap signifies time, and the y-axis represents the pixel number on the vessel. As the plasma is white on a background of black RBCs due to the background fluorescence from GFP, we visualized the plasma moving across the vessel as white stripes on the DMap. As such, velocity (μm/s) was calculated as slope × frames per second/1.6, with 1.6 being the pixel/μm ratio of the recording setting. Measurements of blood flow velocity were calculated by averaging the slope of all collected white stripes in the given period.

Behavioral analysis

To keep data acquisition consistent, all behavioral experiments were performed during the daytime.

EE exploration—Imaging during EE exploration was performed in freely behaving mice. After a baseline was established in the HC, which contained only bedding, mice were moved to an EE cage containing 5–6 objects to freely explore. The EE cage did not include a running wheel, as we did not want exercise to be a confounding factor. Tetrode recordings and blood flow imaging were performed for 70 min of EE exploration or in the HC as a control.

Traveling distance—The traveling distance of mice was recorded and analyzed by EthoVision 14.0 (Noldus Information Technology Inc.). For all EE exploration experiments, we compared the total traveling distance between HC and EE groups for each minute of the 1-h recording. For chemogenetic and pharmacological studies, we plotted the total traveling distance of each 3-min recording session at each time point and compared traveling distance between saline and JHU37160- or L-NAME-injected mice.

Tetrode recording

Neuronal activity was recorded in the dorsal DG in freely moving mice using custom-made tetrodes as previously described(48). Briefly, the tetrode array consisted of eight tetrodes, each having four polyimide-coated nichrome wires (wire diameter: 12.7 µm; Kanthal Palm Coast). The tetrode array targeted the upper granule cell layer (AP: −2.0, ML: 1.3, DV: 1.5 mm) after removal of the dura. A small anchoring stainless screw (shaft diameter: 0.86 mm; length: 4 mm; Fine Science Tools) was used as a reference electrode, which was drilled into the bone above the cerebellum. The tetrode array was then fixed to the skull using dental acrylic cement. Following 1 week of recovery, mice were familiarized with the recording environment. For each recording, mice were placed in the recording room 30 min before recordings to allow them to adapt to the room. Mice were recorded in their HC for 20 min followed by 1 hour of EE or HC as a control. Continuous recording was performed throughout the entire recording procedure, and videos were captured to analyze mouse behavior. The tetrode was lowered down (~40 µm) after each recording to target different cell populations within the DG. After experiments, mice were perfused for confirmation of the tetrode implantation site.

Signals from the dorsal DG were filtered (600–6000 Hz) using Cheetah Data Acquisition software (Neuralynx). Offline analysis was used to isolate the action potentials of single units through the MATLAB-based function MClust (MClust-4.4; A.D. Redish, University of Minnesota, Minneapolis, MN) as previously described(48, 65). In short, single units were classified by similar waveforms through three principal components: peak, valley, and energy. Clusters were manually selected in accordance with waveform similarity and autocorrelograms. To determine the waveform to be analyzed, the average waveform of each channel was quantified, and the largest peak-to-valley amplitude from these channels was applied to produce the peak-to-valley spike width. The ratio of peak amplitude and valley amplitude served as the waveform symmetry index for all units. All isolated single units were grouped by their waveform symmetry ratio, spike width, and long-term firing rate. The long-term firing rate was calculated from the firing rate during the entire recording session. In compliance with previous studies, units that were classified as having low long-term firing rates and low burst index were considered DGCs from excitatory units(66, 67). Burst firing was characterized by counting the number of spikes with intervals <10 ms within each burst.

Chemogenetic and pharmacological studies

We recorded blood flow velocity for 3 min prior to injections for a baseline. Mice in DREADD experiments received saline or JHU37160 (0.5 mg/kg, i.p.; MedChemExpress), and mice in L-NAME experiments received JHU37160 alone or L-NAME (30 µg/g; Sigma-Aldrich, St. Louis, MO) and JHU37160 together. L-NAME was injected 30 min prior to the start of recording, and JHU37160 was injected 10 min before L-NAME. We then recorded blood flow for 3 min every 10 min for a total of 30 min post-injection. JHU37160 was diluted using 10% DMSO and 90% 2-hydroxypropyl-B-cyclodextrin (Cayman Chemical Company; diluted to 20% with saline). For Aβ experiments, L-NAME was provided orally through drinking water at 100 mg/kg, and the water bottles were covered in aluminum foil to prevent light degradation.

Tissue collection and histology

Mice were anesthetized with urethane (200 μg/g) and perfused transcardially with phosphate-buffered saline followed by 4% paraformaldehyde. Brains were extracted and fixed overnight in 4% paraformaldehyde, transferred to a 30% (w/v) sucrose solution, and stored at 4°C until sectioning. Brains were sectioned into 40-μm coronal sections covering the entire anterior/posterior axis of the DG. Sections were stored in cryopreservative until used for immunostaining.

Immunohistochemistry

Sections were first exposed to 0.5% Triton X-100 (PBST) for 10 min for the permeabilization step. We then blocked the sections with 10% donkey serum in 0.25% PBST for 1 h at room temperature. The sections were incubated overnight at 4°C with primary antibody in 0.25% PBST and 3% donkey serum. The primary antibody used in this study was Aβ (rabbit polyclonal anti-human (N-terminal) antibody, 1:250; IBL). The following day, sections were switched to secondary antibody Alexa Fluor 488-conjugated donkey anti-rabbit (1:1000; Jackson Immuno Research) for 3 h while shaking at room temperature. Sections were mounted with DAPI fluoromount, and images were obtained on a Zeiss LSM800 confocal microscope.

Aβ quantification

Brain sections were collected from AppKI mice at different ages, and Aβ immunostaining was performed. We analyzed every eighth hippocampal section. As the DG and CA1 have relatively clear borders but CA2 and CA3 are difficult to distinguish, they were quantified together. We adapted parts of a quantification method published recently(68). Briefly, we outlined the region of interest (ROI) with the polygon function in ImageJ (https://imagej.nih.gov/ij/) while using the Allen Brain Atlas and DAPI counterstain as a guide. Using the measure function, we analyzed the area of the ROI. We then used the color function to remove all colors except for the color used to stain for Aβ. Next, we converted the ROI into 8-bit grayscale and performed the threshold function to determine the area of Aβ in the selected ROI. To ensure that the threshold function did not generate any confounding factors, we stained and imaged all sections to be used in a figure at the same time and kept the threshold level constant. The area fraction option provided us with the percentage of Aβ accumulation in the ROI.

Statistical analysis

Two-way ANOVA was used for the Aβ comparisons shown in Fig. 1, student's t-tests were used to analyze the data shown in Fig. 6 and Supp. Fig. 6, linear mixed models for longitudinal data were used for blood flow analysis, Kruskal–Wallis tests were used for average blood flow velocity fold change and traveling distance comparisons, and Wilcoxon signed-rank tests (paired measurements) or Mann–Whitney tests (unpaired measurements) were used for the remaining comparisons. In the linear mixed models, individual mice were treated as a random effect, and the normality assumption was confirmed. All statistical analyses were conducted with 95% confidence intervals, and p-values of 0.05 were considered as the cutoff for statistical significance. Statistical analysis was performed using

Prism 10.0.3 (GraphPad Software, Boston, Massachusetts). All data are presented as mean ± standard error of the mean (SEM).

Supplementary Material

Refer to Web version on PubMed Central for supplementary material.

Acknowledgments:

We thank Professor Donghui Zhu for critical feedback on the manuscript and Yanyi Mai for assistance with figure illustrations. We also thank all other members of the Ge and Xiong laboratories for their valuable comments. This work was supported by grants R01AG066912 to S.G. and Q.X.; R21AG065864 to S.G.; and R01AG0821471 and P01AG073082 to J.J.P.

Data Availability

The authors confirm that the data supporting the findings of this study are available within the article and its supplementary materials. Raw flow dynamics images were acquired and directly processed using Inscopix Inc. software. All relevant data have been presented in this article. There was no data excluded from the analysis.

References

1. Iadecola C The Neurovascular Unit Coming of Age: A Journey through Neurovascular Coupling in Health and Disease. Neuron. 2017;96(1):17–42. [PubMed: 28957666]
2. Kaplan L, Chow BW, Gu C. Neuronal regulation of the blood–brain barrier and neurovascular coupling. Nature Reviews Neuroscience. 2020;21(8):416–32. [PubMed: 32636528]
3. Rombouts SA, Barkhof F, Veltman DJ, Machielsen WC, Witter MP, Bierlaagh MA, et al. Functional MR imaging in Alzheimer's disease during memory encoding. AJNR Am J Neuroradiol. 2000;21(10):1869–75. [PubMed: 11110539]
4. Dickerson BC, Salat DH, Greve DN, Chua EF, Rand-Giovannetti E, Rentz DM, et al. Increased hippocampal activation in mild cognitive impairment compared to normal aging and AD. Neurology. 2005;65(3):404–11. [PubMed: 16087905]
5. Nippert AR, Biesecker KR, Newman EA. Mechanisms Mediating Functional Hyperemia in the Brain. Neuroscientist. 2018;24(1):73–83. [PubMed: 28403673]
6. Iturria-Medina Y, Sotero RC, Toussaint PJ, Mateos-Pérez JM, Evans AC, Weiner MW, et al. Early role of vascular dysregulation on late-onset Alzheimer's disease based on multifactorial data-driven analysis. Nature Communications. 2016;7(1):11934.
7. Honig LS, Tang MX, Albert S, Costa R, Luchsinger J, Manly J, et al. Stroke and the risk of Alzheimer disease. Arch Neurol. 2003;60(12):1707–12. [PubMed: 14676044]
8. Montagne A, Nikolakopoulou AM, Huuskonen MT, Sagare AP, Lawson EJ, Lazic D, et al. APOE4 accelerates advanced-stage vascular and neurodegenerative disorder in old Alzheimer's mice via cyclophilin A independently of amyloid-β. Nat Aging. 2021;1(6):506–20. [PubMed: 35291561]
9. Wen J, Doerner J, Weidenheim K, Xia Y, Stock A, Michaelson JS, et al. TNF-like weak inducer of apoptosis promotes blood brain barrier disruption and increases neuronal cell death in MRL/lpr mice. Journal of Autoimmunity. 2015;60:40–50. [PubMed: 25911200]
10. Ogawa S, Lee TM, Kay AR, Tank DW. Brain magnetic resonance imaging with contrast dependent on blood oxygenation. Proceedings of the National Academy of Sciences. 1990;87(24):9868–72.
11. Buxton RB, Frank LR. A model for the coupling between cerebral blood flow and oxygen metabolism during neural stimulation. J Cereb Blood Flow Metab. 1997;17(1):64–72. [PubMed: 8978388]
12. Attwell D, Iadecola C. The neural basis of functional brain imaging signals. Trends Neurosci. 2002;25(12):621–5. [PubMed: 12446129]

13. Balbi M, Ghosh M, Longden TA, Jativa Vega M, Gesierich B, Hellal F, et al. Dysfunction of mouse cerebral arteries during early aging. J Cereb Blood Flow Metab. 2015;35(9):1445–53. [PubMed: 26058694]
14. Fabiani M, Gordon BA, Maclin EL, Pearson MA, Brumback-Peltz CR, Low KA, et al. Neurovascular coupling in normal aging: a combined optical, ERP and fMRI study. Neuroimage. 2014;85 Pt 1(0 1):592–607. [PubMed: 23664952]
15. Stefanova I, Stephan T, Becker-Bense S, Dera T, Brandt T, Dieterich M. Age-related changes of blood-oxygen-level–dependent signal dynamics during optokinetic stimulation. Neurobiology of Aging. 2013;34(10):2277–86. [PubMed: 23628145]
16. Topcuoglu MA, Aydin H, Saka E. Occipital cortex activation studied with simultaneous recordings of functional transcranial Doppler ultrasound (fTCD) and visual evoked potential (VEP) in cognitively normal human subjects: effect of healthy aging. Neurosci Lett. 2009;452(1):17–22. [PubMed: 19444940]
17. Zaletel M, Strucl M, Pretnar-Oblak J, Zvan B. Age-related changes in the relationship between visual evoked potentials and visually evoked cerebral blood flow velocity response. Funct Neurol. 2005;20(3):115–20. [PubMed: 16324234]
18. Janik R, Thomason LAM, Chaudhary S, Dorr A, Scouten A, Schwindt G, et al. Attenuation of functional hyperemia to visual stimulation in mild Alzheimer's disease and its sensitivity to cholinesterase inhibition. Biochimica et Biophysica Acta (BBA) - Molecular Basis of Disease. 2016;1862(5):957–65. [PubMed: 26521151]
19. Machulda MM, Ward HA, Borowski B, Gunter JL, Cha RH, O'Brien PC, et al. Comparison of memory fMRI response among normal, MCI, and Alzheimer's patients. Neurology. 2003;61(4):500–6. [PubMed: 12939424]
20. Rosengarten B, Paulsen S, Molnar S, Kaschel R, Gallhofer B, Kaps M. Acetylcholine esterase inhibitor donepezil improves dynamic cerebrovascular regulation in Alzheimer patients. J Neurol. 2006;253(1):58–64. [PubMed: 16096820]
21. Lacroix A, Toussay X, Anenberg E, Lecrux C, Ferreirós N, Karagiannis A, et al. COX-2-Derived Prostaglandin E2 Produced by Pyramidal Neurons Contributes to Neurovascular Coupling in the Rodent Cerebral Cortex. J Neurosci. 2015;35(34):11791–810. [PubMed: 26311764]
22. Ji L, Zhou J, Zafar R, Kantorovich S, Jiang R, Carney PR, et al. Cortical neurovascular coupling driven by stimulation of channelrhodopsin-2. PLoS One. 2012;7(9):e46607. [PubMed: 23029556]
23. Lee JH, Durand R, Gradinaru V, Zhang F, Goshen I, Kim DS, et al. Global and local fMRI signals driven by neurons defined optogenetically by type and wiring. Nature. 2010;465(7299):788–92. [PubMed: 20473285]
24. Anenberg E, Chan AW, Xie Y, LeDue JM, Murphy TH. Optogenetic stimulation of GABA neurons can decrease local neuronal activity while increasing cortical blood flow. J Cereb Blood Flow Metab. 2015;35(10):1579–86. [PubMed: 26082013]
25. Uhlirova H, Kılıç K, Tian P, Thunemann M, Desjardins M, Saisan PA, et al. Cell type specificity of neurovascular coupling in cerebral cortex. Elife. 2016;5.
26. Shen J, Wang D, Wang X, Gupta S, Ayloo B, Wu S, et al. Neurovascular Coupling in the Dentate Gyrus Regulates Adult Hippocampal Neurogenesis. Neuron. 2019;103(5):878–90.e3. [PubMed: 31257104]
27. Palop JJ, Chin J, Roberson ED, Wang J, Thwin MT, Bien-Ly N, et al. Aberrant Excitatory Neuronal Activity and Compensatory Remodeling of Inhibitory Hippocampal Circuits in Mouse Models of Alzheimer's Disease. Neuron. 2007;55(5):697–711. [PubMed: 17785178]
28. Verret L, Mann Edward O, Hang Giao B, Barth Albert MI, Cobos I, Ho K, et al. Inhibitory Interneuron Deficit Links Altered Network Activity and Cognitive Dysfunction in Alzheimer Model. Cell. 2012;149(3):708–21. [PubMed: 22541439]
29. Grouselle D, Winsky-Sommerer R, David JP, Delacourte A, Dournaud P, Epelbaum J. Loss of somatostatin-like immunoreactivity in the frontal cortex of Alzheimer patients carrying the apolipoprotein epsilon 4 allele. Neurosci Lett. 1998;255(1):21–4. [PubMed: 9839717]
30. Sasaki H, Muramoto O, Kanazawa I, Arai H, Kosaka K, Iizuka R. Regional distribution of amino acid transmitters in postmortem brains of presenile and senile dementia of Alzheimer type. Ann Neurol. 1986;19(3):263–9. [PubMed: 2870679]

31. Fukuchi K, Hashikawa K, Seike Y, Moriwaki H, Oku N, Ishida M, et al. Comparison of iodine-123-iomazenil SPECT and technetium-99m-HMPAO-SPECT in Alzheimer's disease. J Nucl Med. 1997;38(3):467–70. [PubMed: 9074540]

32. Meyer M, Koeppe RA, Frey KA, Foster NL, Kuhl DE. Positron emission tomography measures of benzodiazepine binding in Alzheimer's disease. Arch Neurol. 1995;52(3):314–7. [PubMed: 7872887]

33. Hijazi S, Heistek TS, Scheltens P, Neumann U, Shimshek DR, Mansvelder HD, et al. Early restoration of parvalbumin interneuron activity prevents memory loss and network hyperexcitability in a mouse model of Alzheimer's disease. Mol Psychiatry. 2020;25(12):3380–98. [PubMed: 31431685]

34. Lerdkrai C, Asavapanumas N, Brawek B, Kovalchuk Y, Mojtahedi N, Olmedillas Del Moral M, et al. Intracellular Ca(2+) stores control in vivo neuronal hyperactivity in a mouse model of Alzheimer's disease. Proc Natl Acad Sci U S A. 2018;115(6):E1279–e88. [PubMed: 29358403]

35. Palop JJ, Mucke L. Network abnormalities and interneuron dysfunction in Alzheimer disease. Nat Rev Neurosci. 2016;17(12):777–92. [PubMed: 27829687]

36. Lee AJ, Raghavan NS, Bhattarai P, Siddiqui T, Sariya S, Reyes-Dumeyer D, et al. FMNL2 regulates gliovascular interactions and is associated with vascular risk factors and cerebrovascular pathology in Alzheimer's disease. Acta Neuropathol. 2022;144(1):59–79. [PubMed: 35608697]

37. DeTure MA, Dickson DW. The neuropathological diagnosis of Alzheimer's disease. Molecular Neurodegeneration. 2019;14(1):32. [PubMed: 31375134]

38. Xia D, Lianoglou S, Sandmann T, Calvert M, Suh JH, Thomsen E, et al. Novel App knock-in mouse model shows key features of amyloid pathology and reveals profound metabolic dysregulation of microglia. Molecular Neurodegeneration. 2022;17(1):41. [PubMed: 35690868]

39. Rice HC, Marcassa G, Chrysidou I, Horré K, Young-Pearse TL, Müller UC, et al. Contribution of GABAergic interneurons to amyloid-β plaque pathology in an APP knock-in mouse model. Molecular Neurodegeneration. 2020;15(1):3. [PubMed: 31915042]

40. Mucke L, Masliah E, Yu GQ, Mallory M, Rockenstein EM, Tatsuno G, et al. High-level neuronal expression of abeta 1–42 in wild-type human amyloid protein precursor transgenic mice: synaptotoxicity without plaque formation. J Neurosci. 2000;20(11):4050–8. [PubMed: 10818140]

41. Wright AL, Zinn R, Hohensinn B, Konen LM, Beynon SB, Tan RP, et al. Neuroinflammation and neuronal loss precede Aβ plaque deposition in the hAPP-J20 mouse model of Alzheimer's disease. PLoS One. 2013;8(4):e59586. [PubMed: 23560052]

42. Hong S, Quintero-Monzon O, Ostaszewski BL, Podlisny DR, Cavanaugh WT, Yang T, et al. Dynamic analysis of amyloid β-protein in behaving mice reveals opposing changes in ISF versus parenchymal Aβ during age-related plaque formation. J Neurosci. 2011;31(44):15861–9. [PubMed: 22049429]

43. Chiarelli AM, Perpetuini D, Croce P, Filippini C, Cardone D, Rotunno L, et al. Evidence of Neurovascular Un-Coupling in Mild Alzheimer's Disease through Multimodal EEG-fNIRS and Multivariate Analysis of Resting-State Data. Biomedicines. 2021;9(4):337. [PubMed: 33810484]

44. Tarantini S, Tran CHT, Gordon GR, Ungvari Z, Csiszar A. Impaired neurovascular coupling in aging and Alzheimer's disease: Contribution of astrocyte dysfunction and endothelial impairment to cognitive decline. Exp Gerontol. 2017;94:52–8. [PubMed: 27845201]

45. Kisler K, Nelson AR, Montagne A, Zlokovic BV. Cerebral blood flow regulation and neurovascular dysfunction in Alzheimer disease. Nat Rev Neurosci. 2017;18(7):419–34. [PubMed: 28515434]

46. Dimidschstein J, Chen Q, Tremblay R, Rogers SL, Saldi GA, Guo L, et al. A viral strategy for targeting and manipulating interneurons across vertebrate species. Nat Neurosci. 2016;19(12):1743–9. [PubMed: 27798629]

47. Bonaventura J, Eldridge MAG, Hu F, Gomez JL, Sanchez-Soto M, Abramyan AM, et al. High-potency ligands for DREADD imaging and activation in rodents and monkeys. Nature Communications. 2019;10(1):4627.

48. Wang X, Liu H, Morstein J, Novak AJE, Trauner D, Xiong Q, et al. Metabolic tuning of inhibition regulates hippocampal neurogenesis in the adult brain. Proceedings of the National Academy of Sciences. 2020;117(41):25818–29.

49. Shabir O, Pendry B, Lee L, Eyre B, Sharp PS, Rebollar MA, et al. Assessment of neurovascular coupling and cortical spreading depression in mixed mouse models of atherosclerosis and Alzheimer's disease. eLife. 2022;11:e68242. [PubMed: 35014950]
50. Laibaik P, Joan Z, Kenzo K, Gang W, Antoine A, Sung Ji A, et al. tPA Deficiency Underlies Neurovascular Coupling Dysfunction by Amyloid-β. The Journal of Neuroscience. 2020;40(42):8160. [PubMed: 32928888]
51. Bracko O, Cruz Hernández JC, Park L, Nishimura N, Schaffer CB. Causes and consequences of baseline cerebral blood flow reductions in Alzheimer's disease. Journal of Cerebral Blood Flow & Metabolism. 2021;41(7):1501–16. [PubMed: 33444096]
52. Hu WT, Wang Z, Lee VM, Trojanowski JQ, Detre JA, Grossman M. Distinct cerebral perfusion patterns in FTLD and AD. Neurology. 2010;75(10):881–8. [PubMed: 20819999]
53. Alsop DC, Detre JA, Grossman M. Assessment of cerebral blood flow in Alzheimer's disease by spin-labeled magnetic resonance imaging. Ann Neurol. 2000;47(1):93–100. [PubMed: 10632106]
54. Dai W, Lopez OL, Carmichael OT, Becker JT, Kuller LH, Gach HM. Mild cognitive impairment and alzheimer disease: patterns of altered cerebral blood flow at MR imaging. Radiology. 2009;250(3):856–66. [PubMed: 19164119]
55. Yoshiura T, Hiwatashi A, Yamashita K, Ohyagi Y, Monji A, Takayama Y, et al. Simultaneous measurement of arterial transit time, arterial blood volume, and cerebral blood flow using arterial spin-labeling in patients with Alzheimer disease. AJNR Am J Neuroradiol. 2009;30(7):1388–93. [PubMed: 19342545]
56. Zhukov O, He C, Soylu-Kucharz R, Cai C, Lauritzen AD, Aldana BI, et al. Preserved blood-brain barrier and neurovascular coupling in female 5xFAD model of Alzheimer's disease. Front Aging Neurosci. 2023;15:1089005. [PubMed: 37261266]
57. Duncombe J, Lennen RJ, Jansen MA, Marshall I, Wardlaw JM, Horsburgh K. Ageing causes prominent neurovascular dysfunction associated with loss of astrocytic contacts and gliosis. Neuropathology and Applied Neurobiology. 2017;43(6):477–91. [PubMed: 28039950]
58. Shin HK, Jones PB, Garcia-Alloza M, Borrelli L, Greenberg SM, Bacskai BJ, et al. Age-dependent cerebrovascular dysfunction in a transgenic mouse model of cerebral amyloid angiopathy. Brain. 2007;130(9):2310–9. [PubMed: 17638859]
59. Xu Y, Zhao M, Han Y, Zhang H. GABAergic Inhibitory Interneuron Deficits in Alzheimer's Disease: Implications for Treatment. Front Neurosci. 2020;14:660. [PubMed: 32714136]
60. Akama KT, Albanese C, Pestell RG, Van Eldik LJ. Amyloid β-peptide stimulates nitric oxide production in astrocytes through an NFκB-dependent mechanism. Proceedings of the National Academy of Sciences. 1998;95(10):5795–800.
61. Puzzo D, Vitolo O, Trinchese F, Jacob JP, Palmeri A, Arancio O. Amyloid-beta peptide inhibits activation of the nitric oxide/cGMP/cAMP-responsive element-binding protein pathway during hippocampal synaptic plasticity. J Neurosci. 2005;25(29):6887–97. [PubMed: 16033898]
62. Nathan C, Calingasan N, Nezezon J, Ding A, Lucia MS, La Perle K, et al. Protection from Alzheimer's-like disease in the mouse by genetic ablation of inducible nitric oxide synthase. J Exp Med. 2005;202(9):1163–9. [PubMed: 16260491]
63. Cifuentes D, Poittevin M, Bonnin P, Ngkelo A, Kubis N, Merkulova-Rainon T, et al. Inactivation of Nitric Oxide Synthesis Exacerbates the Development of Alzheimer Disease Pathology in APPPS1 Mice (Amyloid Precursor Protein/Presenilin-1). Hypertension. 2017;70(3):613–23. [PubMed: 28760945]
64. Gu Y, Arruda-Carvalho M, Wang J, Janoschka SR, Josselyn SA, Frankland PW, et al. Optical controlling reveals time-dependent roles for adult-born dentate granule cells. Nat Neurosci. 2012;15(12):1700–6. [PubMed: 23143513]
65. Chen L, Wang X, Ge S, Xiong Q. Medial geniculate body and primary auditory cortex differentially contribute to striatal sound representations. Nat Commun. 2019;10(1):418. [PubMed: 30679433]
66. GoodSmith D, Lee H, Neunuebel JP, Song H, Knierim JJ. Dentate Gyrus Mossy Cells Share a Role in Pattern Separation with Dentate Granule Cells and Proximal CA3 Pyramidal Cells. J Neurosci. 2019;39(48):9570–84. [PubMed: 31641051]

67. Neunuebel JP, Knierim JJ. CA3 retrieves coherent representations from degraded input: direct evidence for CA3 pattern completion and dentate gyrus pattern separation. Neuron. 2014;81(2):416–27. [PubMed: 24462102]

68. Christensen A, Pike CJ. Staining and Quantification of β-Amyloid Pathology in Transgenic Mouse Models of Alzheimer’s Disease. Methods Mol Biol. 2020;2144:211–21. [PubMed: 32410038]

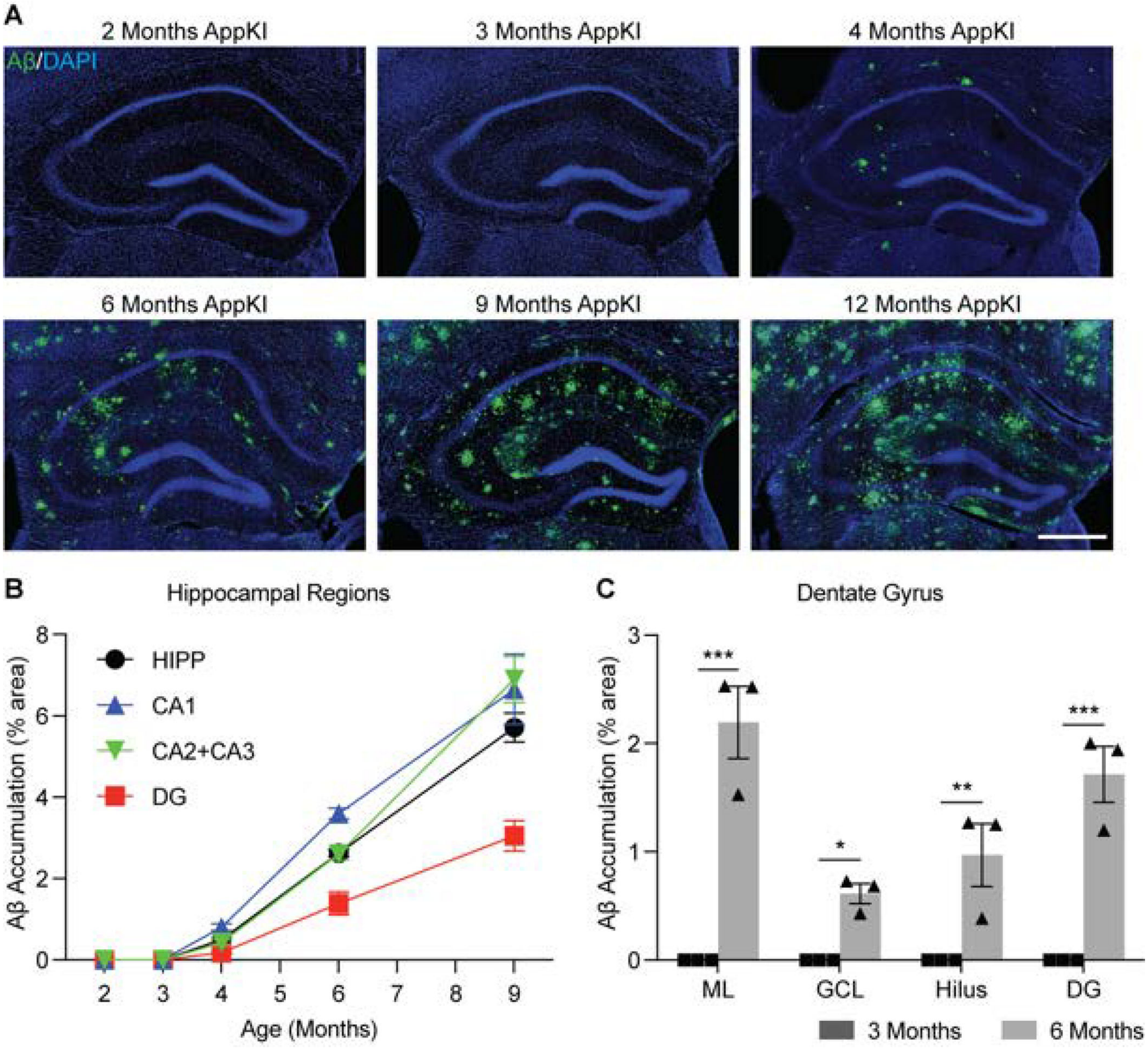

Figure 1.

Aβ accumulation in the hippocampus of AppKI mice during aging

A Representative confocal images of Aβ signal in the hippocampus of 2-, 3-, 4-, 6-, 9- and 12-month-old AppKI mice (scale bar: 500 μm).

B Quantification of Aβ signal by percent area of hippocampal subfields in 2-, 3-, 4-, 6-, and 9month-old AppKI mice (n = 3 mice per age).

C Quantification of Aβ signal by percent area of DG laminae in 3- and 6-month-old AppKI mice (n = 3 mice per age; two-way ANOVA; *p < 0.033, **p < 0.002, ***p < 0.001). Abbreviations: HIPP = hippocampus; ML = molecular layer; GCL = granule cell layer.

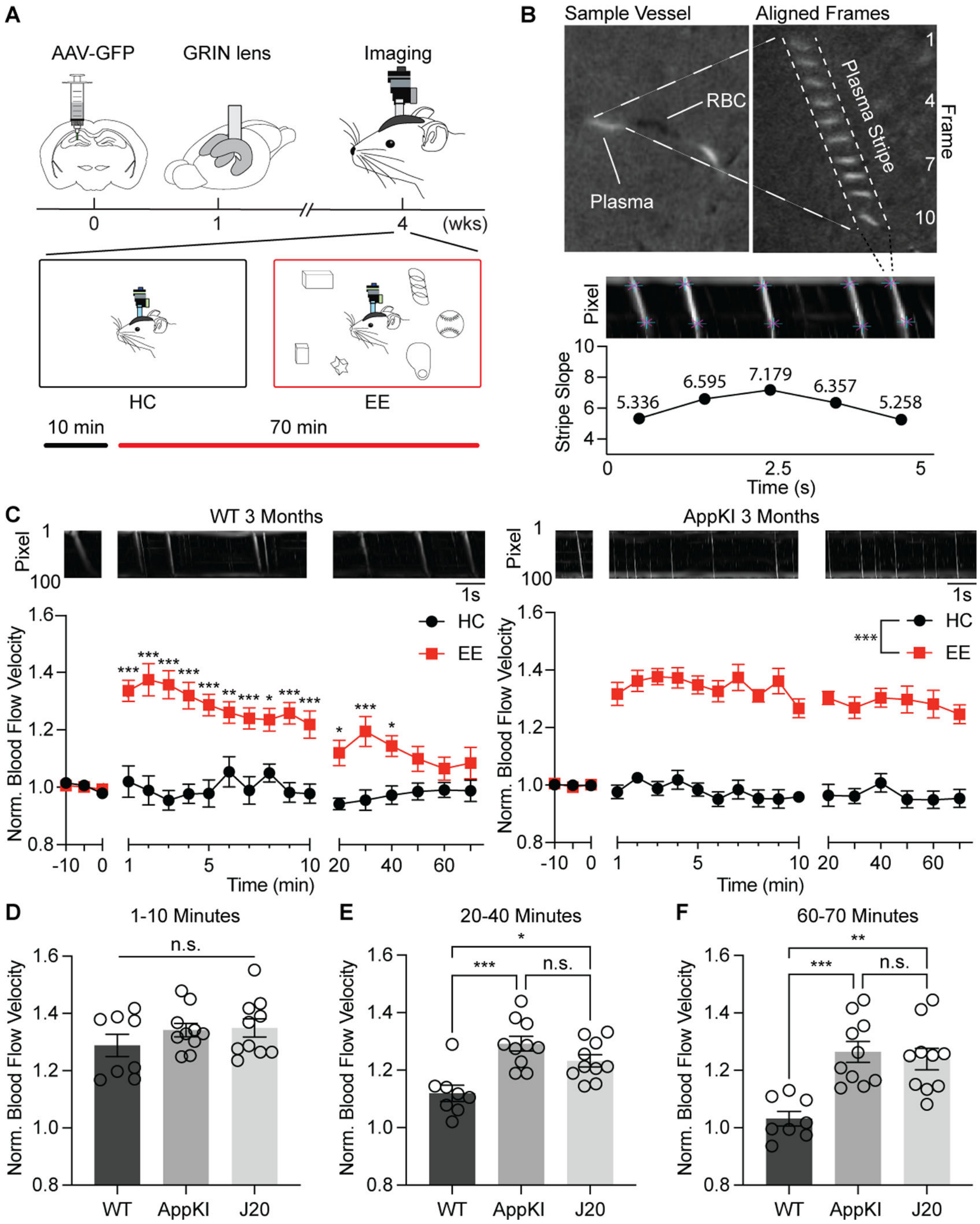

Figure 2.

Context exploration induced hyperemia in the hippocampus of 3-month-old WT and AppKI mice

A Schematics of the surgical procedure for *in vivo* blood flow experiments (top) and recording of microvascular blood flow velocity under HC and EE conditions (bottom) in freely moving mice.

B Example microvessel captured with a miniature microscope (top left). The selected vessel from 10 consecutive frames (60-Hz capturing rate) was aligned to visualize the movement of white plasma (top right). Sample dynamic map (DMap) in which the slope (pixel/frame) of the white plasma stripes represents the measurement of blood flow velocity (bottom).

C Relative blood flow velocity change in 3-month-old WT (left) and AppKI (right) mice during context exploration in EE. Example DMaps of baseline and EE exploration (top) are shown. Baseline recordings were averaged to normalize blood flow velocity in HC (black line, WT: mice = 5, vessels = 8; AppKI: mice = 4, vessels = 10) and EE (red line, WT: mice = 5, vessels = 8; AppKI: mice = 4, vessels = 10). The first 10 min were averaged every 1 min, and the remaining 60 min were recorded for 1 min every 10 min. A linear mixed model for longitudinal data was used to analyze differences between HC and EE. *$p < 0.033$, **$p < 0.002$, ***$p < 0.001$ after Bonferroni adjustment.

D Average blood flow velocity change in each vessel during 1–10 min of EE exploration across different genotypes (vessels: WT = 8, AppKI = 10, J20 = 10; Kruskal–Wallis test; n.s., $p > 0.12$).

E Average blood flow velocity change in each vessel during 20–40 min of EE exploration across different genotypes (vessels: WT = 8, AppKI = 10, J20 = 10; Kruskal–Wallis test; *$p < 0.033$, ***$p < 0.001$, n.s., $p > 0.12$).

F Average blood flow velocity changes in each vessel during 60–70 min of EE exploration across different genotypes (vessels: WT = 8, AppKI = 10, J20 = 10; Kruskal–Wallis test; **$p < 0.002$, ***$p < 0.001$, n.s., $p > 0.12$).

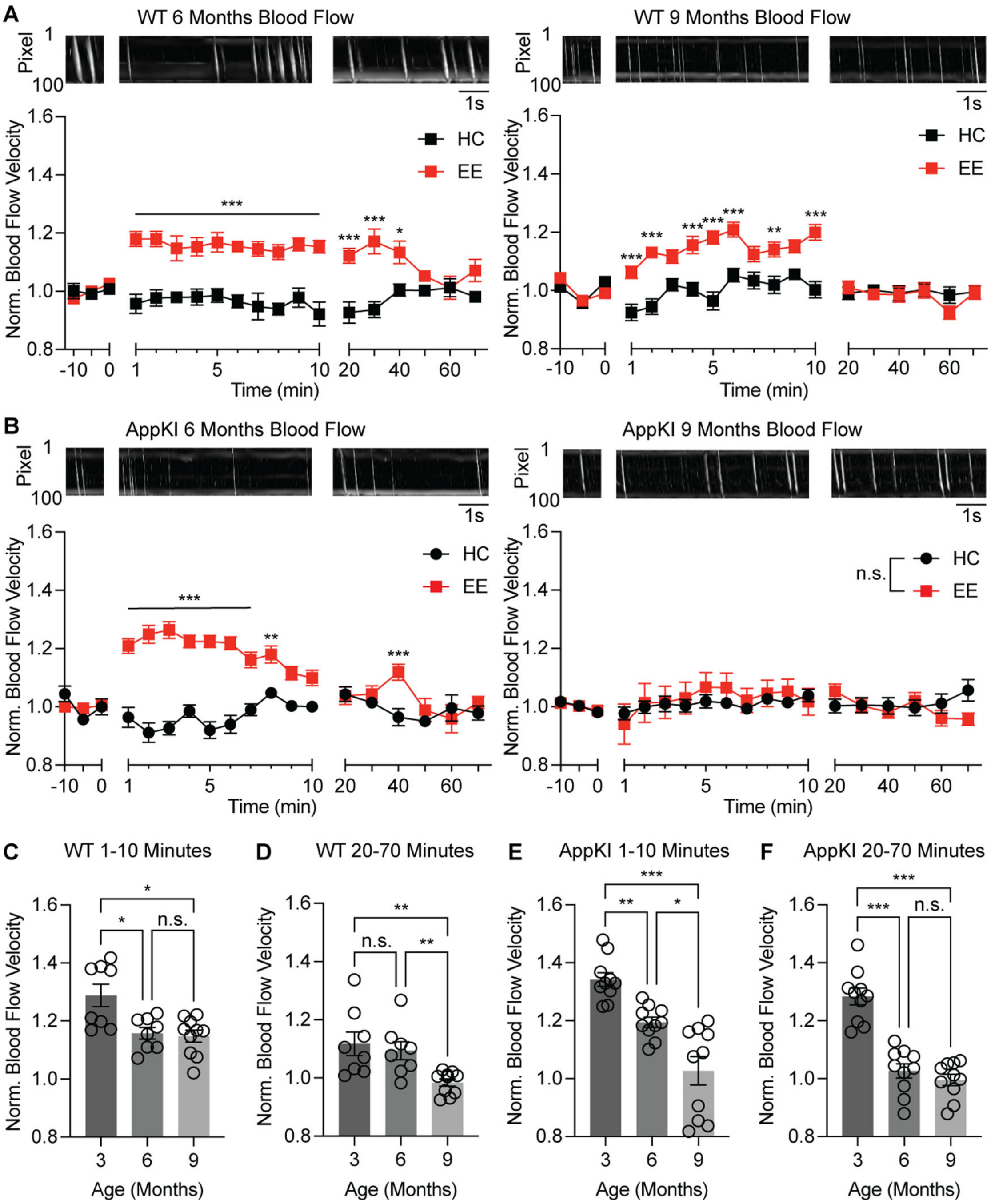

Figure 3.

Context exploration induced hyperemia in the hippocampus of WT and AppKI mice during aging

A Relative blood flow velocity change in 6-month-old WT (left) and 9-month-old WT (right) mice with context exploration in EE. Example DMaps of baseline and EE exploration (top) are shown. Baseline level recordings were averaged to normalize blood flow velocity in HC (black line, 6-month-old: mice = 4, vessels = 8; 9-month-old: mice = 3, vessels = 10) and EE (red line, 6-month-old: mice = 4, vessels = 8; 9-month-old: mice = 3, vessels =

10). The first 10 min were averaged every 1 min, and the remaining 60 min were recorded for 1 min every 10 min. A linear mixed model for longitudinal data was used to analyze differences between HC and EE. *$p < 0.033$, **$p < 0.002$, ***$p < 0.001$ after Bonferroni adjustment.

B Relative blood flow velocity change in 6-month-old AppKI (left) and 9-month-old AppKI (right) mice with contextual exploration in EE. Example DMaps of baseline and EE exploration (top) are shown. Baseline level recordings were averaged to normalize blood flow velocity in HC (black line, 6-month-old: mice = 5, vessels = 10; 9-month-old: mice = 3, vessels = 10) and EE (red line, 6-month-old: mice = 5, vessels = 10; 9-month-old: mice = 3, vessels = 10). The first 10 min were averaged every 1 min, and the remaining 60 min were recorded for 1 min every 10 min. A linear mixed model for longitudinal data was used to analyze differences between HC and EE. **$p < 0.002$, ***$p < 0.001$, n.s., $p > 0.12$ after Bonferroni adjustment.

C Average blood flow velocity change in each vessel during 1–10 min of EE exploration across different ages of WT mice (vessels: 3 months = 8, 6 months = 8, 9 months = 10; Kruskal–Wallis test; *$p < 0.033$, n.s., $p > 0.12$).

D Average blood flow velocity changes in each vessel during 20–70 min of EE exploration across different ages of WT mice (vessels: 3 months = 8, 6 months = 8, 9 months = 10; Kruskal–Wallis test; **$p < 0.002$, n.s., $p > 0.12$).

E Average blood flow velocity change in each vessel during 1–10 min of EE exploration across different ages of AppKI mice (vessels: 3 months = 10, 6 months = 10, 9 months = 10; Kruskal–Wallis test; *$p < 0.033$, **$p < 0.002$, ***$p < 0.001$).

F Average blood flow velocity changes in each vessel during 20–70 minutes of EE exploration across different ages of AppKI mice (vessels: 3 months = 10, 6 months = 10, 9 months = 10; Kruskal–Wallis test; ***$p < 0.001$, n.s., $p > 0.12$).

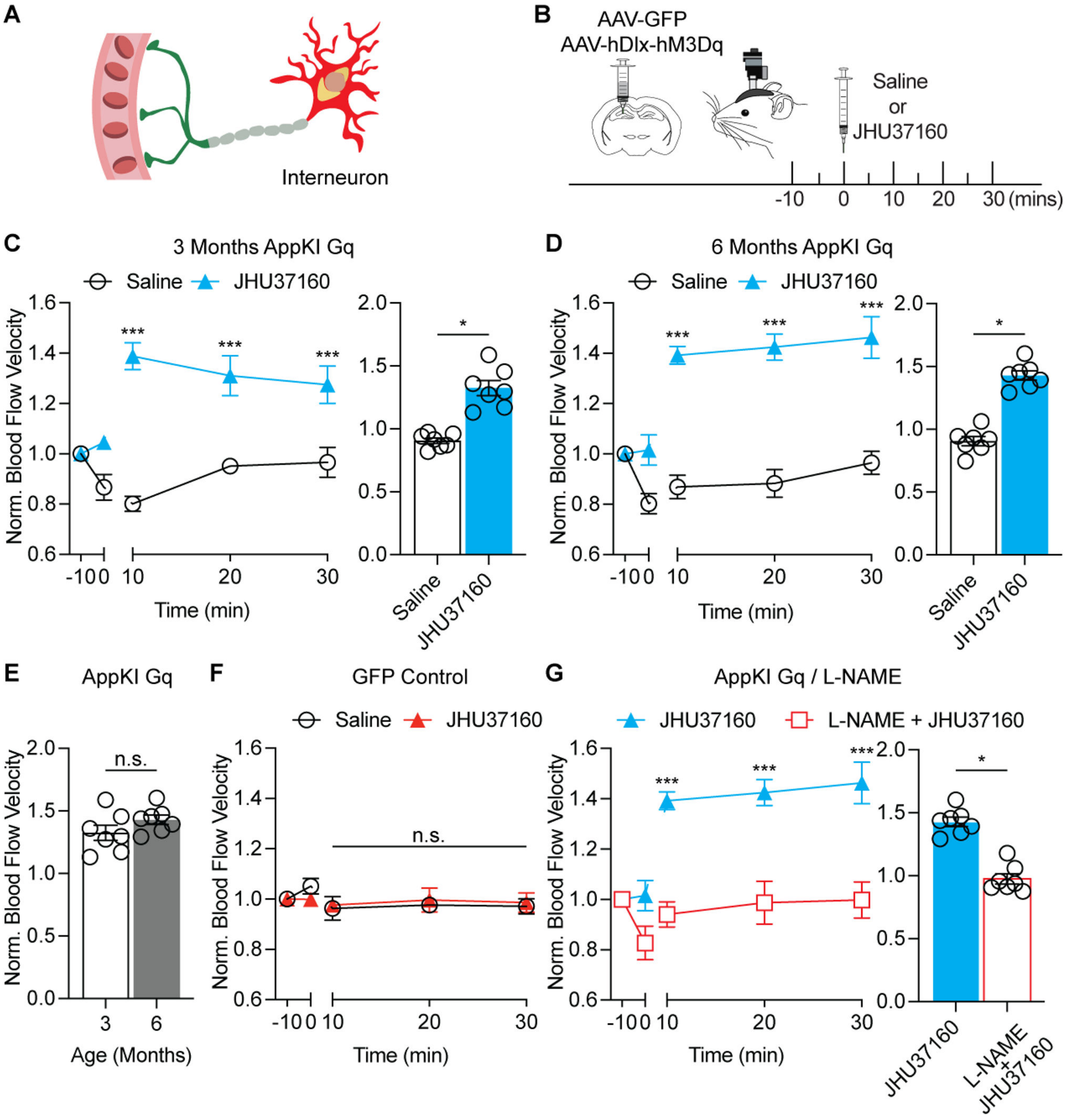

Figure 4.

Chemogenetic activation of hippocampal interneurons induced hyperemia in 3- and 6-month-old AppKI mice

A Illustration of the interaction between interneurons and microvasculature.

B Schematics of the recording timeline of microvascular blood flow velocity with chemogenetic activation of interneurons with JHU37160.

C Left: Chemogenetic activation of hippocampal interneurons in the DG induced functional hyperemia in 3-month-old AppKI mice. Mice were housed in their HC and received saline (black line, mice = 3, vessels = 7) or JHU37160 (blue line, mice = 3, vessels = 7). Each time point was recorded for 3 min, and blood flow velocity was averaged. A linear mixed model for longitudinal data was used to analyze differences between saline and JHU37160. ***p < 0.001 after Bonferroni adjustment. Right: Quantification of average fold change of blood flow velocity 10–30 min post-injection of saline and JHU37160 in 3-month-old AppKI mice (mice = 3, vessels = 7; Wilcoxon signed-rank test; *p < 0.033).

D Left: Chemogenetic activation (Gq) of interneurons in the DG induced functional hyperemia in 6-month-old AppKI mice. Mice were housed in their HC and received saline (black line, mice = 3, vessel = 7) or JHU37160 (blue line, mice = 3, vessel = 7). Each time point was recorded for 3 min, and blood flow velocity was averaged. A linear mixed model for longitudinal data was used to analyze differences between saline and JHU37160. ***p < 0.001 after Bonferroni adjustment. Right: Quantification of average fold change of blood flow velocity 10–30 min post-injection of saline and JHU37160 in 6-month-old AppKI mice (vessels = 7 each; Wilcoxon signed-rank test; *p < 0.033).

E Comparison of average fold change of blood flow velocity 10–30 min post-injection of JHU37160 between 3- and 6-month-old AppKI mice (vessel = 7 each; Mann–Whitney test; n.s., p > 0.12)

F Control experiment on the effect of JHU37160 injection on blood flow velocity in AAV9-CAG-GFP-injected mice. Mice were housed in their HC and received saline (black line, mice = 3, vessels = 5) or JHU37160 (blue line, mice = 3, vessels = 5). Each time point was recorded for 3 min, and blood flow velocity was averaged. A linear mixed model for longitudinal data was used to analyze differences between saline and JHU37160. n.s., p > 0.12 after Bonferroni adjustment.

G Left: L-NAME inhibition of nNOS abolished functional hyperemia induced by chemogenetic activation of hippocampal interneurons in the DG of adult AppKI mice. Mice were housed in their HC and received JHU37160 alone (blue line, mice = 3, vessel = 7) or JHU37160 and L-NAME together (blue line, mice = 3, vessel = 7). Each time point was recorded for 3 min, and blood flow velocity was averaged. A linear mixed model for longitudinal data was used to analyze differences between saline and JHU37160. ***p < 0.001 after Bonferroni adjustment. Right: Quantification of average fold change of blood flow velocity 10–30 min post-injection of JHU37160 alone or JHU37160 and L-NAME together in 6-month-old AppKI mice (vessel = 7 each; Wilcoxon signed-rank test; *p < 0.033).

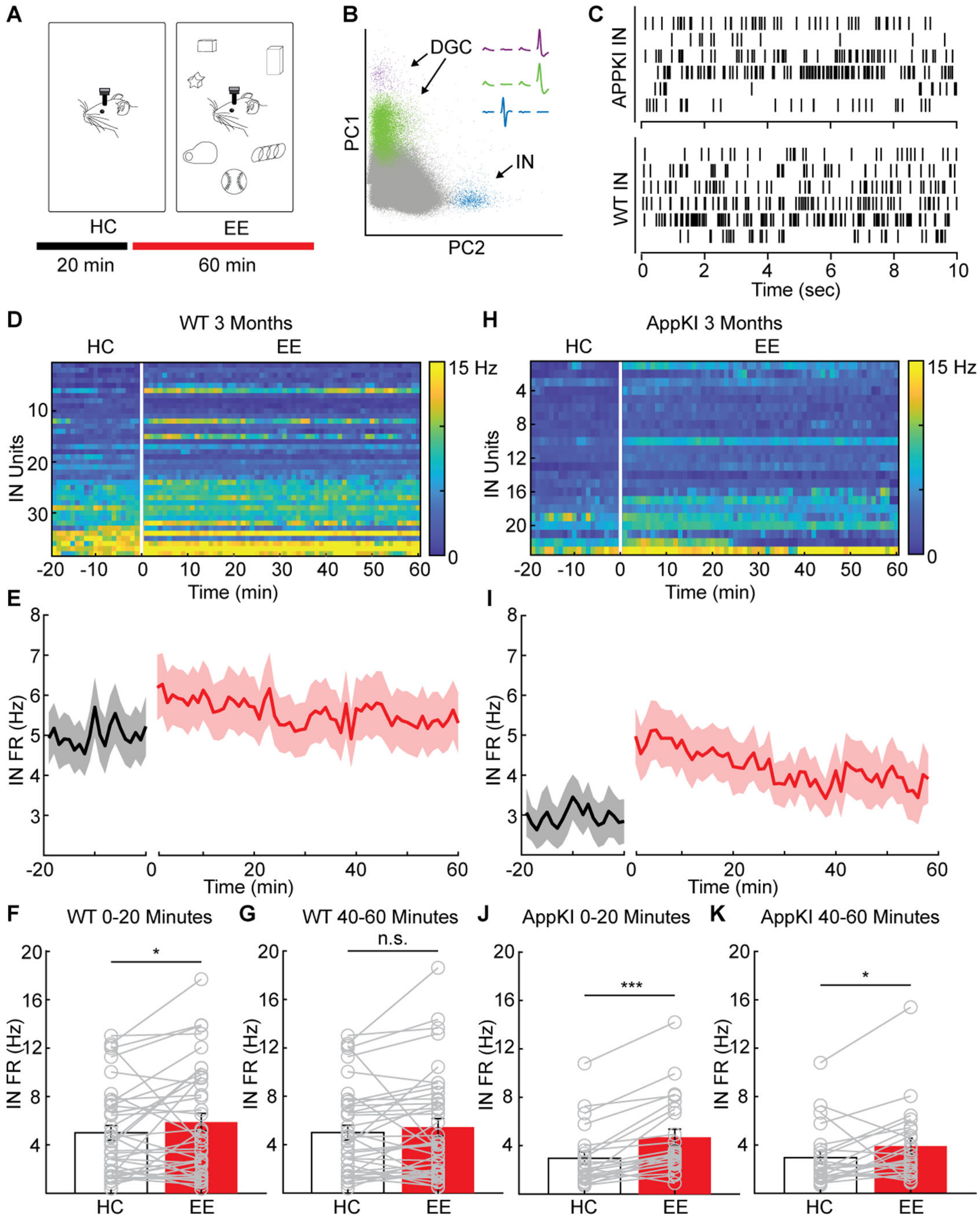

Figure 5.

Context exploration induced activation of hippocampal interneurons in 3-month-old AppKI mice

A Schematic diagram of the experimental paradigm for hippocampal neuronal activity in freely moving mice.

B Schematic drawings of the method used to distinguish between excitatory and inhibitory neurons. Representative waveforms for two DGC units and one interneuron (IN) unit are shown.

C Raster plots of IN unit activities of 3-month-old AppKI (top) and WT (bottom) mice.

D Heatmap showing the firing rate of individual inhibitory units under HC and EE conditions in 3-month-old WT mice.

E Change in average firing rate (FR) of all inhibitory units over time in 3-month-old WT mice.

F Average FR of inhibitory units in HC and 0–20 min of EE in 3-month-old WT mice (units = 38, mice = 3; Wilcoxon signed-rank test; *$p < 0.033$).

G Average FR of inhibitory units in HC and 40–60 min of EE in 3-month-old WT mice (units = 38, mice = 3; Wilcoxon signed-rank test; n.s., $p > 0.12$).

H Heatmap showing the FR of individual inhibitory units under HC and EE conditions in 3-month-old AppKI mice.

I Change in average FR of all inhibitory units over time in 3-month-old AppKI mice.

J Average FR of inhibitory units in HC and 0–20 min of EE in 3-month-old AppKI mice (units = 23, mice = 3; Wilcoxon signed-rank test; ***$p < 0.001$).

K Average FR of inhibitory units in HC and 40–60 min of EE in 3-month-old AppKI mice (units = 23, mice = 3; Wilcoxon signed-rank test; *$p < 0.033$).

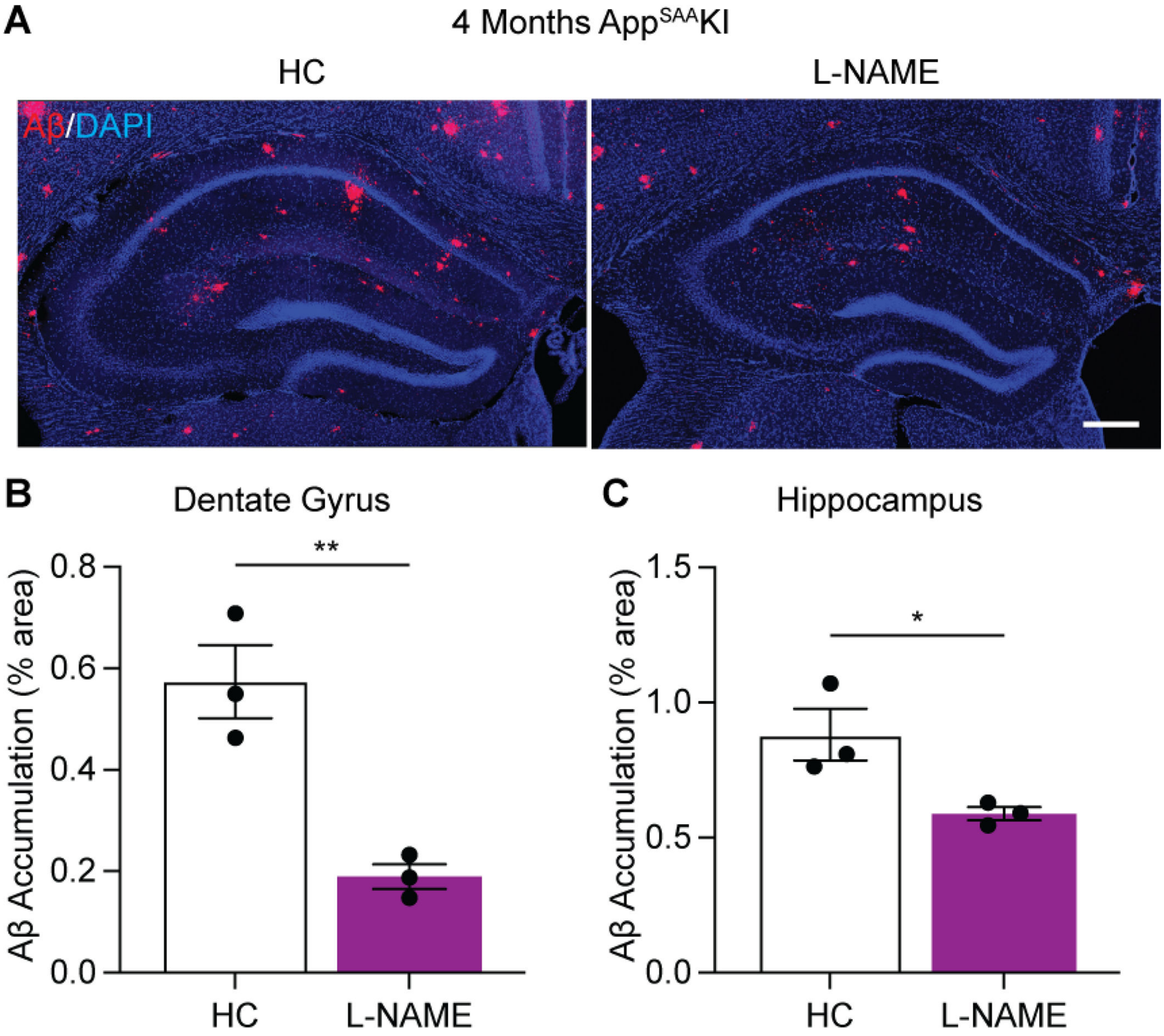

Figure 6.

Effect of EE and suppression of hippocampal neurovascular coupling on Aβ accumulation in 4-month-old AppKI mice

A Representative confocal images showing Aβ accumulation in the hippocampus of 4-month-old AppKI mice under HC, and L-NAME conditions (scale bar: 200 μm).

B Quantification and comparison of Aβ accumulation by percent area of the DG under HC, and L-NAME conditions (mice = 3 per condition; student's t-test; *p<0.05, **p < 0.01).

C Quantification and comparison of Aβ accumulation by percent area of the HIPP under HC, and L-NAME conditions (mice = 3 per condition; student's t-test; *p<0.05, **p < 0.01).